Journal of Functional Materials and Applied Engineering

Research Paper

Construction and Antidrug-Resistant-Bacteria Performance of Nano-Antibacterial Dressings

Richard Taylor [1], Susan Moore [2], Cedric Diggory [2,*]

[1] Industrial Systems Engineering Faculty of Engineering and Applied Sciences, Universityof Regina, Regina, Canada

[2] Department of Chemical and Biological Engineering, Koc University, Rumelifeneri Yolu, Sariyer, 34450, Istanbul, Türkiye

*Corresponding author: Taylor3222@yahoo.com; Moore66@gmail.com; CedricDiggory@gmail.com

Abstract

Black phosphorus (BP) and monolayer MXene/V_2CT_x nanosheets, both prepared via the liquid-phase delamination method, were mixed to fabricate MXene/BP composite (AC) by a hydrothermal method. Characterization of the composite was carried out with SEM, TEM, XRD, and a multi-angle particle-size and high-sensitivity zeta-potential analyzer. The resulting AC was then incorporated into poly(lactic-co-glycolic acid) (PLGA), from which nano-antibacterial dressings (PLGA-AC) were produced via electrospinning. The dressings were tested by SEM and an optical contact-angle measuring instrument. In-vitro antibacterial assays, in-vitro cell culture experiments and hemolysis tests were performed to evaluate the reactive oxygen species (ROS)-generating capacity, antibacterial activity and biocompatibility of PLGA-AC. The results show that monolayer MXene nanosheets are homogeneously distributed on the BP surface, and the two components are combined by van der Waals forces. PLGA-AC exhibits excellent hydrophilicity with a water contact angle of 52.05°. Under ultrasonic irradiation, PLGA-AC possesses outstanding ROS-generating capacity, achieving a clearance rate of over 99 % against *Escherichia coli*. PLGA-AC also displays favorable cytocompatibility and blood compatibility, with a hemolysis rate of merely 0.97 % toward rabbit red blood cells.

Keywords: *MXene; black phosphorus; composites; electrospinning; antibacterial performance; pharmaceutical raw materials*

Received on 02 July 2024, Accepted on 05 Nov 2024, Published on 15 Dec 2024

1 Introduction

Over the past several decades, antibiotic therapy has been the primary treatment for bacterial infections[1-2]. The widespread misuse of antibiotics, however, has driven the rise of drug-resistant bacterial strains, endangering public health on a broad scale. Because such strains withstand the action of nearly all available antibiotics, the arsenal of treatments for bacterial infections in humans has been drastically narrowed[3-4]. Although new antibiotics targeting diverse drug-resistant bacteria have been discovered, their application may accelerate bacterial mutation and drive the evolution of multidrug-resistant strains[5]. Therefore, effective non-antibiotic strategies are urgently required for antibacterial therapy of wounds infected by drug-resistant bacteria.

In the context of infected-wound management, antibacterial strategies that do not rely on antibiotics have lately drawn intense research interest, since such agents combine potent bactericidal action with a low propensity to induce resistance[6]. Among the externally activated modalities explored so far, photodynamic therapy (PDT) has been the most extensively studied: upon illumination at an appropriate wavelength, a photosensitizer generates reactive oxygen species (ROS) that destroy bacteria. Its usefulness, however, is confined to shallow lesions because light can only penetrate a limited depth into tissue, which severely hampers clinical translation. Sonodynamic therapy (SDT) has therefore emerged as an attractive alternative, relying on ultrasound-triggered piezoelectric fields as controllable, non-invasive stimuli. The ability of ultrasound to reach deep tissue makes SDT particularly appealing for treating deeply infected cutaneous wounds[10-11]. Through the cavitation effect,

ultrasound nucleates bubbles that act as physical triggers and, upon collapsing, release intense localized stress[12]. When piezoelectric materials are subjected to this cavitation-induced stress, they swiftly develop internal electric fields and surface piezopotentials. The resulting surface potential conveys mechanical energy across the material's surface or the material–solution interface, driving carrier transport and initiating a variety of redox reactions[13-14]. This ultrasound-to-energy conversion can further be coupled with nanozyme catalysis, thereby transforming surrounding molecular oxygen into ROS capable of eliminating bacteria.

Among emerging sono-piezoelectric candidates, the two-dimensional material black phosphorus (BP) has garnered considerable interest from researchers[15-16]. Featuring biocompatibility and biodegradable degradation products, BP acts as an attractive candidate two-dimensional sonopiezoelectric material. Benefiting from its piezoelectric properties, BP can induce ROS generation under ultrasound irradiation to realize antibacterial effects[17-18]. Unfortunately, pure BP suffers from low electron-hole separation efficiency and low ROS yield, which severely restrict its application in antibacterial fields. He et al.[19] and Jin et al.[20] adopted multiple routes to improve its catalytic performance, including morphology regulation, element doping and heterojunction construction. Composites assembled from two distinct components with different energy-level and band-gap configurations (semiconductor or metallic) can realize comprehensive SDT therapy by coordinating their band structures and chemical compositions[21].

Recent years have witnessed remarkable progress in technologies for skin regeneration, and a variety of platforms — including hydrogels, microspheres, 3D-printed scaffolds, and electrospun fibrous scaffolds — have been explored for constructing wound dressings that promote skin repair[22]. Of these, electrospun scaffolds stand out as especially promising for wound healing, benefiting from their extensive specific surface area and highly porous architecture. Electrospun dressings share many similarities with extracellular matrix structures and can provide favorable physiological microenvironments for wound regeneration. Furthermore, Rnjak-Kovacina et al.[23] reported that porous scaffolds fabricated by electrospinning can facilitate cell adhesion and proliferation.

In this work, hydrothermal technology was adopted to fabricate intelligent nano-antibacterial composite (AC) consisting of BP and monolayer MXene(V_2CT_x). AC can rapidly generate ROS for antibacterial purposes under ultrasonic treatment. AC was further integrated with poly(lactic-co-glycolic acid) (PLGA) by electrospinning to prepare composite wound dressings. This study aims to obtain wound dressings with excellent biocompatibility and bactericidal performance, and provide new ideas and theoretical foundations for antibacterial therapy.

2 Experimental Section

2.1 Reagents and Instruments

Drug-resistant Escherichia coli (DEC, ATCC 25922) was obtained from Wuhan Walna Biotechnology Co., Ltd., while peptone and beef extract came from Beijing Aobao Biotechnology Co., Ltd. Mouse fibroblast L929 cells were sourced from the American Type Culture Collection, and DMEM medium containing 10 wt% fetal bovine serum was supplied by Thermo Fisher Scientific (USA). The immunostaining permeabilization reagent (0.1 vol% Triton X-100 in PBS) was purchased from Shanghai Beyotime Biotechnology Co., Ltd. FITC-conjugated phalloidin, 4',6-diamidino-2-phenylindole (DAPI), rabbit red blood cells, PLGA with a number-average molecular weight (Mn=80000), and analytical-grade HCl and LiF were all acquired from Beijing Solarbio Science & Technology Co., Ltd. V_2CT_x-MAX (the precursor of MXene(V_2CT_x), BP, NaCl, and LB agar medium were provided by Chengdu Kelong Chemicals Co., Ltd.; Tris-HCl buffer by Beijing Taiyang Biotechnology Co., Ltd.; 1,1,1,3,3,3-hexafluoro-2-propanol (HFIP), methylene blue (MB) solution (100 mg/L), 25 mg/L glutaraldehyde aqueous solution, and absolute ethanol by Shanghai Aladdin Biochemical Technology Co., Ltd.; OsO_4 (10 mg/L) and uranyl acetate by Merck Chemicals (Shanghai) Co., Ltd., Chengdu Branch; and phosphate-buffered saline (PBS, pH=8.5) together with 4 vol% paraformaldehyde by Sigma-Aldrich (Shanghai) Trading Co., Ltd. All deionized water used in the experiments was prepared in the laboratory.

The characterization instruments used in this study included a JSM-7610F field-emission scanning electron microscope (SEM) and a JEM-F200 field-emission transmission electron microscope (TEM), both from JEOL, Japan;

an XRD-7000S X-ray diffractometer (XRD) from Shimadzu, Japan; a MultiMode 8-HR atomic force microscope (AFM) from Bruker, Germany; an SL200B optical contact-angle goniometer from KINO Instruments, USA; a UV-1800PC UV-Vis spectrophotometer from Shanghai Aoxi Scientific Instrument Co., Ltd.; a TCS SP8 laser scanning confocal microscope (CLSM) from Leica, Germany; and an Omni multi-angle particle-size and high-sensitivity zeta-potential analyzer from Brookhaven Instruments, USA.

2.2 Preparation Procedures

2.2.1 Fabrication of Composite Material

Liquid-phase exfoliation was employed to obtain BP nanosheets: 30 mg of BP powder was dispersed into 100 mL of deionized water under a nitrogen blanket, sonicated for 12 h, and then centrifuged at 3000 r/min for 3 min, affording a BP nanosheet suspension at a concentration of roughly 0.2 g/L.

Monolayer MXene(V2CTx)nanosheets were fabricated following a previously reported route[24]. In brief, 1 g of (V2CTx)-MAX precursor was etched in a solution prepared from 1 g of LiF and 20 mL of 9 mol/L HCl, with continuous stirring maintained at 40 °C for 24 h. The resulting MXene powder underwent repeated washing and centrifugation, and subsequent freeze-drying at −20 °C for 12 h delivered the monolayer MXene nanosheets.

Hydrothermal route was adopted for composite preparation. 2 mg monolayer MXene nanosheets were added into 100 mL as-prepared BP nanosheet suspension. After 1 h of stirring, the solution was sealed in a 100 mL autoclave and subjected to hydrothermal reaction at 120 °C for 3 h. The solid product was then washed and lyophilized under vacuum at −20 °C for 12 h, yielding roughly 15 mg of the final black composite powder, hereafter referred to as AC.

2.2.2 Fabrication of Nano-Dressings

A spinning dope was prepared by dispersing 200 mg of the composite powder together with 1 g of PLGA in 10 mL of HFIP over 12 h. Electrospinning was then performed with a 20 cm needle-to-collector gap, a solution feed rate of 0.02 mL/min, and an applied voltage of 15.0 kV. Fibers were deposited at room temperature onto a cylindrical collector rotating at 1 mm/min, and the resulting electrospun dressing is referred to as PLGA-AC.

Following identical experimental steps, BP nanosheets and monolayer MXene nanosheets were used to replace composite powder to prepare reference samples named PLGA-BP and PLGA-MXene, respectively. Pure PLGA dressing was fabricated without adding composite powder.

2.3 Characterization and Performance Tests

XRD test: Cu target, tube voltage 40 kV, tube current 40 mA, Kalpha wavelength 0.15444 nm, scanning rate 10 (°)/min, scanning range 3°–90°. SEM test: accelerating voltage 10 kV, gold-sputtering pretreatment for samples. TEM test: sample dispersion droplets were cast onto copper grids, operating voltage 200 kV.

Sonodynamic-performance test: Hydroxyl-radical generation was quantified by MB using UV-Vis spectrophotometer. Different dressings were immersed in 200 µL MB solution (100 mg/L). Samples were incubated for 15 min under static conditions, followed by 15 min ultrasonic treatment. After centrifugation, UV-Vis absorption spectra of different samples were recorded within the wavelength range of 450–750 nm.

2.4 Determination of In-Vitro Antibacterial Activity

2.4.1 Drug-Resistance Evaluation of DEC

Co-culture of DEC with amoxicillin of different mass concentrations and spread-plate method were adopted to characterize drug-resistance of DEC. Specifically, DEC suspension was diluted with LB medium to prepare bacterial suspension of $1*10^4$ CFU/mL. 500 µL bacterial suspension was transferred into each well of 48-well plates. Amoxicillin was supplemented to individual wells at mass concentrations of 0, 50.0, 125.0, 250.0, 312.5 mg/L, followed by 15 min incubation. From every well, a 35 µL aliquot of the treated bacterial suspension was taken and spread uniformly over LB agar plates, which were subsequently kept at 37 °C for 24 h until distinct colonies became visible.

2.4.2 Spread-Plate Culture Assay

The in-vitro antibacterial efficacy of the electrospun dressings was examined using drug-resistant E. coli as the model organism. Four samples — PLGA, PLGA-MXene, PLGA-BP, and PLGA-AC dressings — were compared initially by the spread-plate assay. Each dressing was sectioned into 1cm*1 cm squares and placed into the wells of a 48-well plate, with parallel sets assigned to ultrasound-treated and static conditions. An E. coli suspension adjusted to $1*10^5$ CFU/mL with LB medium was dispensed into the wells at 500 μL per well. Samples in the ultrasound set were irradiated for 15 min at a power density of 1.5 W/cm^2, whereas those in the static set were simply left to stand for the same duration. Finally, 35 μL of the suspension from each well was spread onto LB agar plates and cultured at 37 °C for 24 h, after which visible colonies were enumerated.

2.4.3 Bacterial Morphology Observation

Morphological alterations of the drug-resistant bacteria following the various treatments were examined by TEM. To prepare specimens, 1 mL of bacterial culture from each dressing-treated condition (with and without ultrasound) was harvested by centrifugation at 8000 r/min for 10 min. The cells were first fixed in 2.5 vol% glutaraldehyde for 2 h and post-fixed in OsO_4solution (10 mg/L). Dehydration was carried out through a graded ethanol series — 30, 50, 70, 90, and 100 vol% — with 10 min at each step, followed by uranyl acetate staining. The finished sections were then placed on copper grids for TEM imaging.

2.5 In-Vitro Biocompatibility Evaluation

2.5.1 Cell Culture

L929 cells were cultured in DMEM medium in an incubator under 37 °C, 90 % relative humidity and 5 vol % CO_2 atmosphere. Experiments were conducted when cell confluence reached 85 %.

2.5.2 Observation of Cell Morphology and Cytoskeleton

For morphological examination, L929 cells seeded at $1* 10^4$ cells per well were grown alongside the different dressings in 48-well plates for 24 h. Thereafter, the cells were fixed with 2.5 vol% glutaraldehyde for 2 h and dehydrated through a graded ethanol series (30, 50, 70, 90, and 100 vol%, 20 min at each level). Once air-dried, the specimens were imaged by SEM.

The cytoskeletal organization of the L929 cells was further probed by immunofluorescence staining. In this assay, cells ($1*10^4$ per well) were cultured on glass coverslips placed in 48-well plates, with 500 μL of medium added to each well. Fixation was performed with 4 vol% paraformaldehyde for 0.5 h, followed by rinsing with PBS. The fixed cells were then permeabilized for 20 min using 0.1 vol% Triton X-100 in PBS and washed again with PBS. F-actin was visualized with FITC-conjugated phalloidin and nuclei were counterstained with DAPI, and fluorescence images of every sample were recorded by CLSM.

2.6 Hemolytic-Activity Assay

Different dressings were incubated with rabbit red blood cells, and hemolysis rate was calculated. Firstly, dressings (1 cm* 1 cm） were placed in 1.5 mL EP tubes. 50 μL red-blood-cell suspension (5 vol % in PBS) was added into each tube. PBS served as negative control, and deionized water served as positive control. Following a 1 h incubation at 37 °C, the samples were spun at 3500 r/min for 10 min, after which the absorbance of the supernatant was read at 540 nm. The hemolytic activity of the dressings was expressed as the hemolysis rate (%), computed from Equation (1): Hemolysis rate/%=（A-A0)/A100-A0)* 100 Where: A, A0 and A100 represent absorbance values of sample group, negative-control group and positive-control group, respectively.

3 Results and Discussion

3.2 Design, Preparation and Characterization of Composite Material

Figure 1 shows the schematic diagram for synthetic route and sonogenic antibacterial mechanism of AC and PLGA-AC.

Figure 1 Schematic diagram of synthesis route and sonogenic antibacterial process of AC and PLGA-AC

As illustrated in Figure 1, monolayer MXene obtained via liquid-phase delamination was transferred into an autoclave and fully contacted with BP nanosheets in liquid phase. The two components assembled into AC driven by van der Waals forces. Afterwards, AC was loaded into electrospun membranes by electrospinning technology to obtain nano-antibacterial dressings. The resultant dressings can release abundant ROS upon ultrasonic stimulation and effectively eradicate drug-resistant bacteria.

Figure 2 presents SEM and AFM images of MXene and BP.

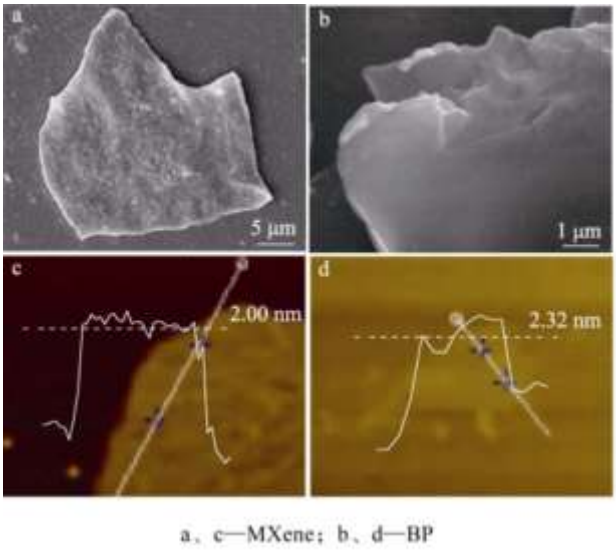

Figure 2 SEM (a, b) and AFM (c, d) images of MXene and BP a, c — MXene; b, d — BP

Figure 2a and 2b demonstrate that both MXene and BP exhibit sheet-like monolayer structures. According to Figure 2c and 2d, the thicknesses of MXene and BP nanosheets are approximately 2.00 nm and 2.32 nm, close to their theoretical values of 1.50 nm and 2.00–5.00 nm, respectively.

Figure 3 displays SEM image of AC and EDS elemental mapping of O, C, P, V.

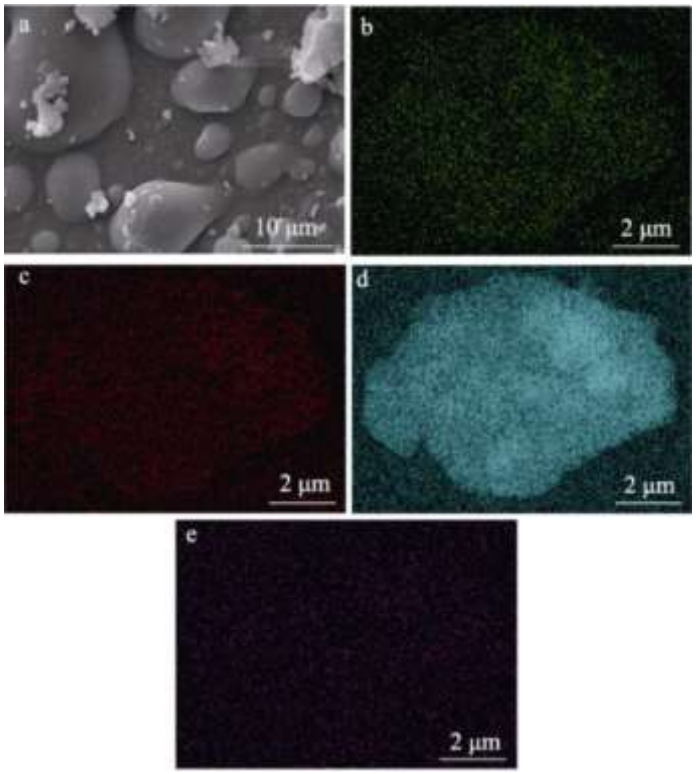

Figure 3 SEM image of AC (a) and EDS element distribution mapping of O (b), C (c), P (d), V (e)

It can be observed from Figure 3 that MXene and BP nanosheets are homogeneously dispersed on AC surfaces, constructing structures with large specific surface area. The presence of O, C, P and V elements confirms uniform distribution of MXene nanosheets on BP substrates.

Figure 4 shows XRD patterns of MXene, BP and AC.

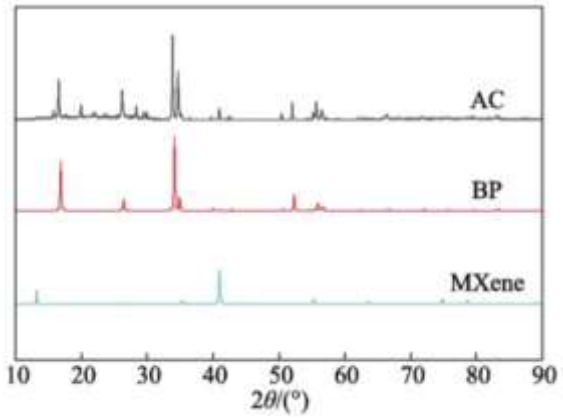

Figure 4 XRD patterns of BP, MXene and AC

As shown in Figure 4, characteristic diffraction peaks of AC at 2theta=34.202°, 35.000 °, 56.852 ° and 40.951 ° correspond to the (040), (111), (132) crystal planes of BP and the (102) crystal plane of MXene, verifying successful fabrication of AC. The combination of MXene and BP does not alter the crystal structure of AC, which excludes the possibility that crystal structures dominate the catalytic activity of AC.

Figure 5 summarizes zeta-potential test results of MXene, BP and AC.

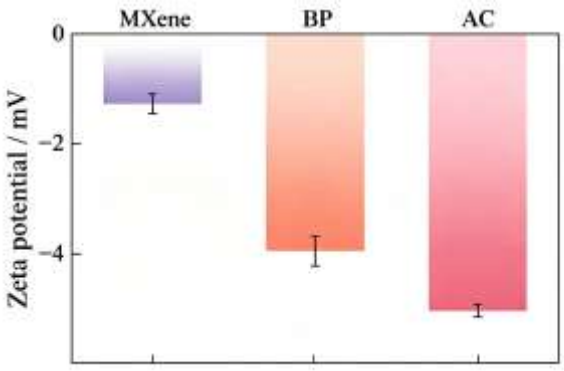

Figure 5 Zeta potential of BP, MXene and AC

From Figure 5, MXene surfaces carry negative charges due to robust terminal functional groups on MXene. The zeta potential of AC roughly equals the sum of zeta potentials of MXene and BP. This phenomenon originates from tight connection between MXene and BP via van der Waals forces and homogeneous dispersion of MXene nanosheets on BP surfaces.

3.2 Characterization and Hydrophilic-Performance Analysis of Antibacterial Dressings

Figure 6 shows SEM micrographs of PLGA dressing, PLGA-BP, PLGA-MXene and PLGA-AC.

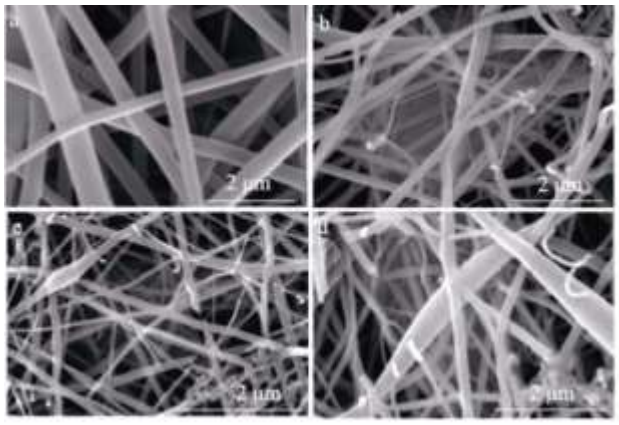

Figure 6 SEM images of PLGA dressing (a), PLGA-BP (b), PLGA-MXene (c) and PLGA-AC (d)

As can be seen in Figure 6, all fibers exhibit random orientation, smooth morphology, interconnected porous architectures and comparable fiber diameters. BP, MXene and AC are dispersed within PLGA-BP, PLGA-MXene and PLGA-AC samples, respectively.

Since surface wettability strongly influences how well a wound-repair material supports cell growth and tissue regeneration, the hydration behavior of the samples was characterized by water-contact-angle (WCA) analysis. The WCA data for the PLGA dressing, PLGA-BP, PLGA-MXene, and PLGA-AC are summarized in Figure 7.

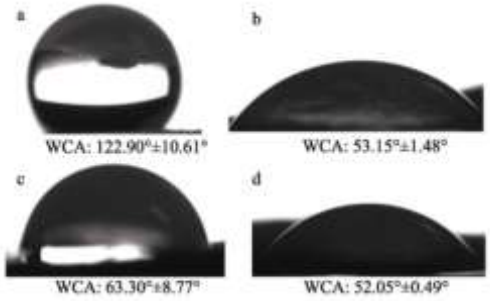

Figure 7 Water contact angle of PLGA dressing (a), PLGA-BP (b), PLGA-MXene (c) and PLGA-AC (d)

PLGA dressing shows relatively hydrophobic property with WCA of 122.90 ° (Figure 7a). After modification with BP or MXene, WCA values of PLGA-BP and PLGA-MXene decrease significantly to 53.15 ° and 63.30^ °. PLGA-AC delivers the lowest WCA of 52.05 °, which is largely attributed to the introduction of hydrophilic phosphorus and vanadium elements. These findings demonstrate that the PLGA-AC surface is hydrophilic in nature, a property favorable to fibroblast attachment and differentiation and thus indicative of the material's promise in wound-repair applications.

3.3 ROS-Generating-Performance Analysis of Antibacterial Dressings

MB assay enables qualitative determination of ROS yield. ROS can react with MB and induce decolorization, accompanied by decreased absorbance near 660 nm. In MB tests, hydroxyl radicals react with MB cations to produce OH^- and MB radical cations[25]. Since MB cations are deep-blue while MB radical cations are colorless, the reaction between MB and hydroxyl radicals causes color fading from deep blue to colorless and reduced absorbance, so that ROS content can be quantified[26]. Figure 8 presents UV-Vis absorption spectra of MB for PLGA dressing, PLGA-BP, PLGA-MXene and PLGA-AC under ultrasonic treatment.

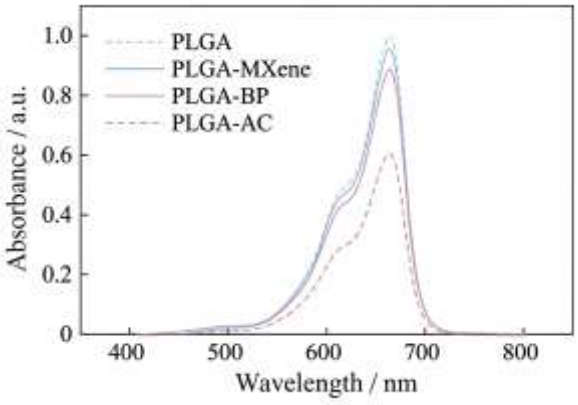

Figure 8 UV-Vis adsorption spectra of MB of PLGA dressing, PLGA-BP, PLGA-MXene and PLGA-AC under ultrasound

As shown in Figure 8, upon ultrasonic stimulation, PLGA-MXene hardly generates detectable changes. The absorbance values of PLGA-BP and PLGA-AC are far lower than those of pure PLGA dressing. This is because efficient separation of electrons and holes occurs inside composites, and oxygen from ambient atmosphere is captured to produce ROS. Notably, under identical ultrasonic conditions, the absorbance peak height of PLGA-AC is slightly lower than that of PLGA-BP, demonstrating that the construction of composite AC further improves ROS yield. ROS are mainly derived from the BP component inside AC. As a sonopiezoelectric material, the conduction-band (CB) edge of BP shifts toward negative potential and its valence-band (VB) edge shifts upward under ultrasound irradiation, enhancing redox capability[27]. MXene, the other constituent of composite AC, not only has large specific surface area but also displays metal-like high conductivity and accelerates rapid surface-electron transfer[28]. Therefore, sonogenerated electrons can rapidly transfer from BP to MXene,

simultaneously promoting massive production of negatively charged electrons and positively charged holes. This process triggers rapid ROS generation and elevates ROS yield of antibacterial composites. Hence, constructing composite AC favors ROS production under ultrasonic irradiation.

3.4 Drug-Resistant-Bacteria-Inhibiting Performance of Antibacterial Dressings

Figure 9 displays drug-resistance test results of DEC. From Figure 9, abundant bacterial colonies still exist after DEC is co-incubated with amoxicillin at mass concentration of 312.5 mg/L, which confirms the drug-resistant property of DEC[29].

Figure 9 Bacterial colony pictures of DEC after co-cultured by amoxicillin with different mass concentrations

Figure 10 shows spread-plate antibacterial test results of ultrasound group and static group for PLGA dressing, PLGA-BP, PLGA-MXene and PLGA-AC. In Figure 10, comparable colony growth is observed for ultrasound group and static group of PLGA dressing, proving that pure PLGA dressing has no bactericidal capacity. No obvious differences are found among static groups of PLGA dressing, PLGA-MXene, PLGA-BP and PLGA-AC, indicating these dressings cannot suppress DEC proliferation without ultrasonic stimulation. After 15 min ultrasonic treatment, significantly decreased colony-forming units (CFU) are observed for ultrasound groups of PLGA-BP and PLGA-AC. PLGA-AC can effectively kill DEC by generating large amounts of ROS, which further verifies that ROS are mainly originated from BP component inside AC, consistent with Figure 8 results. Without antibiotics, PLGA-AC achieves persistent clearance activity against drug-resistant DEC with antibacterial rate higher than 99 %.

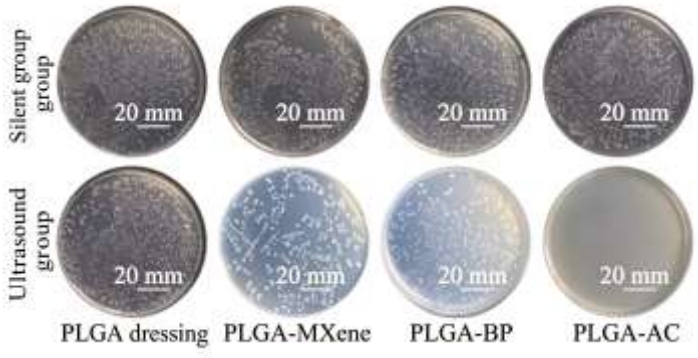

Figure 10 Bacterial colony pictures of DEC treated with different dressings

Figure 11 gives TEM images of intracellular and extracellular structures and organelles of DEC for static PLGA-AC group and ultrasound-treated PLGA-AC group. As shown in Figure 11, DEC in static PLGA-dressing group retains intact cell wall and cytoplasm with compact intracellular structures (DNA, cytoplasm). By contrast, DEC from ultrasound-treated PLGA-AC group suffers severe damage and deformation. Its cell walls are disrupted, cytoplasm leaks out, intracellular regions turn into vesicular structures and DNA is completely destroyed. The results demonstrate that PLGA-AC possesses powerful potential for eradicating pathogenic microorganisms under ultrasonic irradiation, in accordance with spread-plate assay results. A possible mechanism is that bacteria adhere onto surfaces of antibacterial nanofibers, and their structural integrity is destroyed under subsequent ultrasonic stimulation.

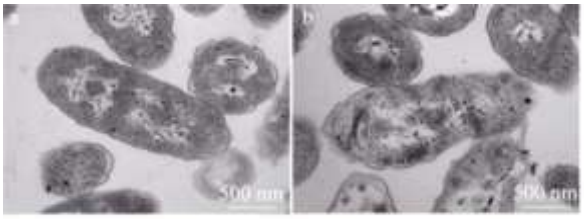

Figure 11 TEM images of DEC after contact PLGA dressing without ultrasound (a) and PLGA-AC with ultrasound (b)

3.5 Cytocompatibility Evaluation of Antibacterial Dressings

Apart from strong bactericidal capability, biocompatibility constitutes another vital indicator for wound-repair materials. Figure 12 and Figure 13 exhibit SEM and CLSM images of L929 cells incubated on PLGA-BP, PLGA-MXene and PLGA-AC.

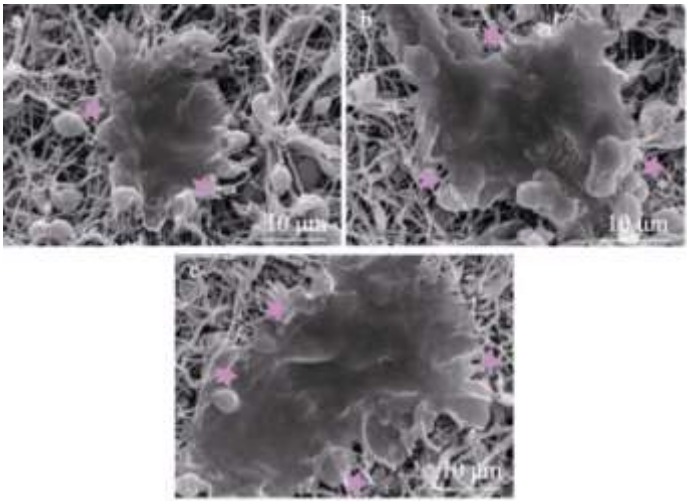

Figure 12 SEM images of L929 cells incubated on PLGA-BP (a), PLGA-MXene (b) and PLGA-AC (c)

From Figure 12, after 24 h co-culture with PLGA-BP, PLGA-MXene and PLGA-AC, L929 cells present spread morphology and tightly attach to all samples via filopodia (marked by purple asterisks), indicating favorable cell-adhesion performance. Especially for PLGA-AC group (Figure 12c), porous features of the sample provide advantageous anchoring sites for cell adhesion.

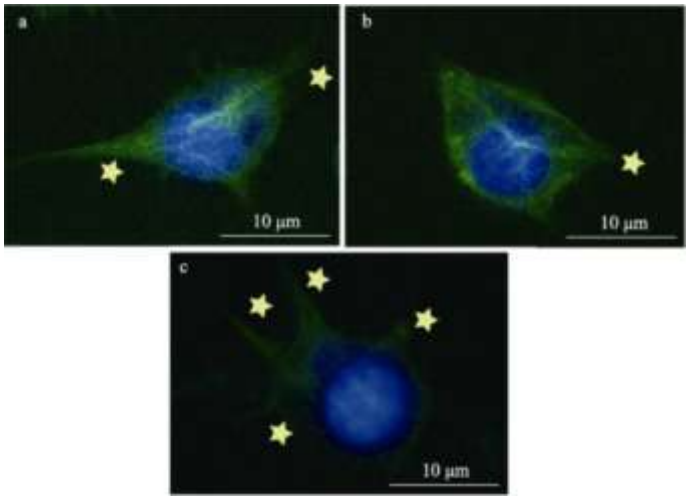

Figure 13 CLSM maps of L929 cells incubated on PLGA-BP (a), PLGA-MXene (b) and PLGA-AC (c)

CLSM images further validate above observations. In the fluorescence images of Figure 13, DAPI renders the nuclei blue, while the cytoskeleton appears green owing to labeling with FITC-conjugated phalloidin.

Compared with L929 cells on PLGA-BP (Figure 13a) and PLGA-MXene (Figure 13b), L929 cells treated by PLGA-AC (Figure 13c) spread better and develop more mature F-actin. Such behavior likely stems from the favorable combination of pronounced hydrophilicity and suitable surface roughness in PLGA-AC, both of which create conditions conducive to cell attachment and growth, confirming that the dressing is well tolerated by cells.

3.6 Blood-Compatibility Analysis of Antibacterial Dressings

Hemolysis denotes the breakdown of red blood cells (RBCs), a process through which hemoglobin and other intracellular constituents escape into the surrounding milieu. Hemolytic property serves as another key index for biosafety evaluation of biomaterials. Figure 14 summarizes hemolysis-rate test results of PLGA dressing, PLGA-BP, PLGA-MXene and PLGA-AC.

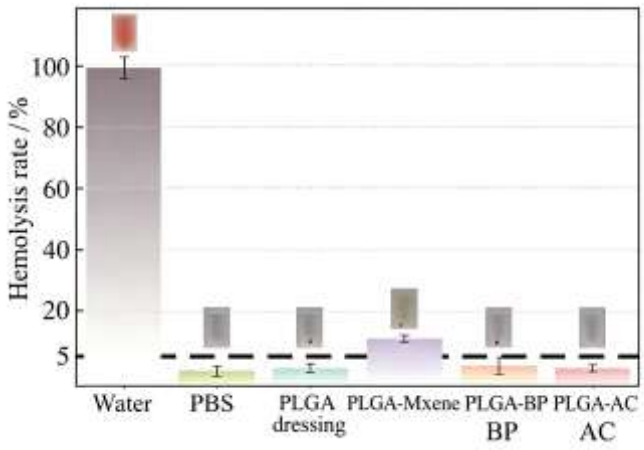

Figure 14 Hemolysis rate of different dressings Inset: corresponding representative physical photographs

From Figure 14, hemolysis rates of positive-control (water), negative-control (PBS), PLGA, PLGA-MXene, PLGA-BP and PLGA-AC groups are 100.00 %, 0 %, 1.10 %, 10.34 %, 1.93 % and 0.97 %, respectively. Red blood cells treated by PLGA-AC remain non-hemolytic and show nearly no distinction compared with PBS negative control, demonstrating its excellent blood compatibility.

In this work, hydrothermally synthesized MXene/BP composite (AC) was integrated into electrospun PLGA fibrous scaffolds to construct sonodynamic nano-antibacterial dressings (PLGA-AC), addressing the urgent challenge of drug-resistant bacterial wound infection without relying on conventional antibiotics. The enhanced therapeutic performance originates from rational heterostructure construction, optimized interfacial electron transfer, favorable physicochemical surface properties and ultrasound-triggered reactive oxygen species (ROS) generation.

Pure black phosphorus (BP), as a sonopiezoelectric two-dimensional material, can produce ROS under ultrasonic stimulation, yet it suffers from low electron-hole separation efficiency and limited ROS output, which restricts its practical antibacterial efficacy. By assembling monolayer V_2CT_x MXene nanosheets onto BP surfaces via van der Waals interactions through a hydrothermal reaction, the AC heterostructure forms uniform sheet-on-sheet architecture with large specific surface area. Characterizations including SEM-EDS, XRD and zeta-potential analysis confirm homogeneous distribution of MXene over BP substrates while preserving the intrinsic crystal structures of both two-dimensional components. Metallic MXene acts as an efficient electron sink owing to its outstanding electrical conductivity. Upon ultrasound irradiation, mechanical cavitation stress induces piezopotential inside BP, shifting its conduction-band and valence-band positions to strengthen redox capacity.

Photo-generated electrons rapidly migrate from BP to adjacent MXene nanosheets across the heterointerfaces, effectively suppressing the recombination of electron-hole pairs. This accelerated charge separation substantially elevates ROS production yield, which is validated by methylene-blue decolorization tests. Therefore, the synergistic coupling between BP sonopiezoelectric effect and MXene conductive charge-transport capability constitutes the core mechanism for boosted sonodynamic activity.

After incorporating AC composite into electrospun PLGA fibers, the resultant PLGA-AC dressing maintains interconnected porous fibrous morphology similar to extracellular matrix. Compared with hydrophobic pure PLGA membrane (water contact angle 122.90°), the introduction of phosphorus- and vanadium-rich AC greatly improves surface hydrophilicity, lowering the water contact angle to 52.05°±0.49°. Such improved wettability provides favorable anchoring sites for fibroblast attachment, spreading and cytoskeleton maturation, as demonstrated by SEM and confocal laser-scanning microscopy observations of L929 mouse fibroblasts. Benefiting from optimized surface properties, PLGA-AC achieves desirable cytocompatibility without obvious cytotoxicity. Moreover, its hemolysis rate is only 0.97 %, comparable to the negative PBS control, proving satisfactory blood compatibility for wound-contact applications.

In-vitro antibacterial experiments against drug-resistant Escherichia coli (DEC) reveal that PLGA-AC shows negligible bacteriostatic effects under static conditions. Once triggered by ultrasound, abundant ROS released from the dressing oxidizes bacterial components, disrupting cell wall integrity, inducing cytoplasmic leakage and destroying intracellular DNA structures. Consequently, PLGA-AC achieves over 99 % clearance efficiency toward drug-resistant bacteria in antibiotic-free circumstances. In summary, the hydrothermally built MXene/BP heterostructure facilitates charge separation and amplifies sonodynamic ROS output. When embedded within porous hydrophilic PLGA electrospun networks, the composite dressing combines potent ultrasound-activated sterilization and excellent biosafety. This material design offers a feasible non-antibiotic strategy for treating wounds infected by drug-resistant bacteria.

4 Conclusions

(1) Nano-antibacterial dressing PLGA-AC was fabricated by hydrothermal method combined with electrospinning technology. The electrospun fibers possess smooth appearance, interconnected porous structures and uniform fiber diameters. The dressing exhibits excellent hydrophilicity with WCA of \(52.05^\circ\pm0.49^\circ\), and can promote cell adhesion and proliferation.
(2) PLGA-AC can continuously generate ROS under ultrasonic stimulation so as to realize effective inhibition of pathogenic bacteria. Antibacterial assays show that PLGA-AC achieves persistent clearance activity against drug-resistant DEC in antibiotic-free environments, with antibacterial rate higher than 99 %.
(3) In-vitro cell experiments verify favorable biocompatibility of PLGA-AC, which possesses great application potential for cutaneous-wound therapy with drug-resistant-bacteria infection.
The as-prepared nano-antibacterial dressing PLGA-AC integrates outstanding antibacterial capacity and favorable biocompatibility, and is expected to be applied as wound-repair dressing for infected skin.

References

[1] WANG J H, TIAN T, LI J C, et al. Research progress on removal of antibiotic resistant bacteria and genes in water by photochemical AOPs[J]. Fine Chemicals, 2021, 38(5): 889-897.
[2] WEI X L, GAO J, WANG F, et al. In situ capture of bacterial toxins for antivirulence vaccination[J]. Advanced Materials, 2017, 29(33): 1701644.
[3] JANSEN K U, KNIRSCH C, ANDERSON A S. The role of vaccines in preventing bacterial antimicrobial resistance[J]. Nature Medicine, 2018, 24(1): 10-19.
[4] TANG Y L, WANG L P, LU L X, et al. Research progress of enzymatic biological modified antibacterial materials[J]. Fine Chemicals, 2023, 40(3): 465-477.
[5] BLASKOVICH M A, HANSFORD K A, GONG Y, et al. Protein-inspired antibiotics active against vancomycin- and daptomycin-resistant bacteria[J]. Nature Communications, 2018, 9(1): 22.
[6] HUI A P, YANG F F, KANG Y R, et al. High pressure homogenization assisted fabrication of CTAB modified plant essential oil/palygorskite antibacterial composites[J]. Fine Chemicals, 2021, 38(10): 2019-2024, 2033.

[7] ZHONG K P, ZHANG Z F, CHENG W Y, et al. Photodynamic O_2 economizer encapsulated with dnazyme for enhancing mitochondrial gene-photodynamic therapy[J]. Advanced Healthcare Materials, 2024, 13(5): 2302495.
[8] CHANG G R, LU X Y, PEI C, et al. Application of ZnPc loaded macroporous silica nanocarrier in the photodynamic therapy[J]. Fine Chemicals, 2018, 35(3): 388-394.
[9] ZHOU X, WANG Z, CHAN Y K, et al. Infection micromilieu-activated nanocatalytic membrane for orchestrating rapid sterilization and stalled chronic wound regeneration[J]. Advanced Functional Materials, 2022, 32(7): 2109469.
[10] WANG X, DAI X Y, CHEN Y. Sonopiezoelectric nanomedicine and materdicine[J]. Small, 2023, 19(29): 2301693.
[11] WANG R H, LIU Q W, GAO A, et al. Recent developments of sonodynamic therapy in antibacterial application[J]. Nanoscale, 2022, 14(36): 12999-13017.
[12] WANG Q Q, TIAN Y, YAO M, et al. Bimetallic organic frameworks of high piezovoltage for sono-piezo dynamic therapy[J]. Advanced Materials, 2023, 35(41): 2301784.
[13] SONG X R, ZHANG Q, CHANG M Q, et al. Nanomedicine-enabled sonomechanical, sonopiezoelectric, sonodynamic and sonothermal therapy[J]. Advanced Materials, 2023, 35(31): 2212259.
[14] HUA M Y, WU R H, CHEN W Y, et al. Ultrasound-activated piezocatalyst triggers sulfate radical production for augmented oxidative tumor suppression[J]. Small Structures, 2023, 5(4): 2300461.
[15] LI Z Y, ZHANG T M, FAN F, et al. Piezoelectric materials as sonodynamic sensitizers to safely ablate tumors: A case study using black phosphorus[J]. The Journal of Physical Chemistry Letters, 2020, 11(4): 1228-1238.
[16] MA W D, LU J F, WAN B S, et al. Piezoelectricity in multilayer black phosphorus for piezotronics and nanogenerators[J]. Advanced Materials, 2020, 32(7): 1905795.
[17] LIU Y J, LI Z Y, FAN F, et al. Boosting antitumor sonodynamic therapy efficacy of black phosphorus via covalent functionalization [J]. Advanced Science, 2021, 8(20): 2102422.
[18] ZHANG W H, YU L T, JIANG Y, et al. Phycocyanin-functionalized black phosphorus quantum dots enhance PDT/PTT therapy by inducing ROS and irreparable DNA damage[J]. Biomaterials Science, 2021, 9(15): 5302-5318.
[19] HE M M, WANG Z Y, YANG H, et al. Multi-functional bio-enzyme: Revolutionizing diabetic skin regeneration with its glucose-unlocked sterilization and programmed anti-inflammatory effects[J]. Advanced Science, 2023, 10(21): 2300986.
[20] JIN Z L, WANG T, CUI E T, et al. Constructing a tandem heterojunction: S-scheme heterojunction and ohmic junction based on graphdiyne, synergistically optimizing photocatalytic hydrogen evolution[J]. Chemical Engineering Journal, 2023, 477: 147210.
[21] HUANG Y L, HUANG Y X, WANG Z Y, et al. Engineered bio-heterojunction with infection-primed H_2S liberation for boosted angiogenesis and infectious cutaneous regeneration[J]. Small, 2023, 19(45): 2304324.
[22] CHOUHAN D, DEY N, BHARDWAJ N, et al. Emerging and innovative approaches for wound healing and skin regeneration: Current status and advances[J]. Biomaterials, 2019, 216: 119267.
[23] RNJAK-KOVACINA J, WEISS A S. Increasing the pore size of electrospun scaffolds[J]. Tissue Engineering Part B: Reviews, 2011, 17(5): 365-372.
[24] ZHANG J C, GAO X Y, MA D C, et al. Copper ferrite heterojunction coatings empower polyetheretherketone implant with multi-modal bactericidal functions and boosted osteogenicity through synergistic photo/fenton-therapy[J]. Chemical Engineering Journal, 2021, 422: 130094.
[25] WIEDMER D, SAGSTUEN E, WELCH K, et al. Oxidative power of aqueous non-irradiated TiO_2-H_2O_2 suspensions: Methylene blue degradation and the role of reactive oxygen species[J]. Applied Catalysis B: Environmental, 2016, 198: 9-15.
[26] SATOH A Y, TROSKO J E, MASTEN S J. Methylene blue dye test for rapid qualitative detection of hydroxyl radicals formed in a Fenton's reaction aqueous solution[J]. Environmental Science & Technology, 2007, 41(8): 2881-2887.
[27] LI Z Y, ZHANG T M, FAN F, et al. Piezoelectric materials as sonodynamic sensitizers to safely ablate tumors: A case study using black phosphorus[J]. The Journal of Physical Chemistry Letters, 2020, 11(4): 1228-1238.
[28] LI B, LUO Y, ZHENG Y F, et al. Two-dimensional antibacterial materials[J]. Progress in Materials Science, 2022, 130: 100976.
[29] PANDEY A, AFSHEEN A, TIWARI S K. Isolation and characterization of multi drug resistance cultures from waste water[J]. Journal of Pharmacy and Bioallied Sciences, 2011, 13(13): 1-7.